World Journal of Environmental Biosciences

Available Online at: **www.environmentaljournals.org**

Volume 8, Issue 4: 42-57

ISSN 2277- 8047

Sr-Nd Isotope Constraints of Hezar Igneous Complex (south of Kerman- Iran) - as a Part of Urumieh-Dokhtar Magmatic Arc

Mohammad Noorizadeh[1]*, Abbas Moradian[2], Hamid Ahmadipour[2], Mohammad Reza Ghassemi[3], José Francisco Santos[4]

[1] Neyshabur Technical College, Technical & Vocational University, Tehran, Iran.
[2] Department of Geology, Faculty of Science, Shahid Bahonar University of Kerman, Kerman, Islamic Republic of Iran
[3] Research Institute for Earth Sciences, Geological Survey of Iran, Meraj Ave., Azadi Sq., Tehran, Islamic Republic of Iran
[4] Department of Geosciences, Geobiotec Research Unit, University of Aveiro, 3810-193 Aveiro, Portugal.

ABSTRACT

The Hezar Igneous Complex (HIC) in the south-eastern part of Urumieh-Dokhtar magmatic arc, is the most prominent magmatic feature in the Kerman Porphyry Copper Belt, near Rayen, south of Kerman. It is indicated that the possible place of the vent is in Jalas Mountain which has been split later by the Sabzevaran fault into Minor and Major Jalas. The sub-alkaline rocks of this complex are mainly composed of different pyroclastic and lava flow rocks, acidic to basic in composition. Positive Epsilon Nd values and low Sr in HIC, besides TDM 0.6-0.7 Ga indicates formation from partial melting of lithospheric mantle sources which is modified with previous subduction components. Positive epsilon Nd indicates that these rocks have been originated from evolved magmas without assimilation of crustal materials. All of the samples except two cases are far from mantle array which indicates that they are located in mantle wedge over the subduction zone and subjected to some increasing in $^{87}Sr/^{86}Sr$ ratios. The depicted isochron for three related samples indicates an age of 47±5 Ma with MSWD=0.44 which is an indication for the main magmatic activity of this complex. But two other samples give an unreliable age of 6.4 Ma for some intrusive bodies (dikes) in Jalas which is the last phase of magmatism in HIC.

Keywords: *Strontium-neodymium isotopic analysis, Volcanic arc, Igneous complex, Rayen, Kerman.*

Corresponding author: Mohammad Noorizadeh
e-mail ✉ nooorizad @ gmail.com
Received: 22 April 2019
Accepted: 28 September 2019

1. INTRODUCTION

Urumieh-Dokhtar Magmatic Arc (UDMA) as a part of Central Iran, is located in the middle of the Alpine-Himalayan belt. UDMA, parallel with other parts of Zagros structural zone with an NW-SE trend, is the product of the convergence and interaction between Eurasia/Laurasia and Gondwana. UDMA is a linear magmatic belt related to subduction which is constituted with huge volcanic successions with minor plutonic rocks along the active margin of the Iranian plate. This magmatic arc, for a long time, has been interpreted as an Andean type magmatic arc of the subduction of Neotethyan oceanic lithosphere under Iranian plate. During the subduction of Neotethyan oceanic lithosphere under the Central Iran microcontinent, UDMA has been an active continental margin (Kananian et al., 2014 and other references not included).

During the opening of Neotethys in Permian to early Jurassic, some continental fragments (Turkey, Iran, Tibet, and Indochina) from the northern margin of Gondwana was rifted and drifted to the north. These microcontinents collided to the Eurasian margin in different parts making a complex set of archipelagos. Evolution of UDMA is related to the successive stages of the closure of Tethys including its subduction during Cretaceous-Oligocene and its continent-continent collision in Paleogene – Neogene (Alimohammadi, Alirezaei and Kontak, 2015 and references therein).

Rayen tourist town is one of the ancient regions of Kerman province which is located in 100 km SE of Kerman and 1079 km SE of Tehran. Many domestic and foreign tourists come to these touristic towns (Moshfe et al., 2017). The studied area, Hezar Igneous Complex (HIC), which is located at the west of Rayen, between 29°25′00″N, 57 10′00″E and 29°35′00″N, 57 25′00″E, is a part of Dehaj-Sarduyieh volcanic belt and is located in the southern part of the UDMA and south-western part of the 1/100.000 geological map of Rayen in Figure 1 (Dimitrijevic, 1973).

In three recent decades, ecological issues (Dayani Tilaki et al., 2018) and its maintatance have drawn global attention more than before (Suvorov et al., 2018). Besides its significance in ecotourism of the region (Noorizadeh et al., 2018; Noorizadeh et al., 2013), HIC plays also a significant role in geological interpretation of the region:

The subduction of the Neotethys is broadly considered as the key process acting from Jurassic to Tertiary not only in UDMA but also in Sanandaj-Sirjan Zone (SSZ) and caused arc magmatism (Chiu et al., 2013). This study may add a significant piece of data to the complex puzzle of the region. Besides, Kerman Cenozoic Magmatic Arc (KCMA) with one of the most important copper deposits of the world is associated with Miocene porphyries which both are intruded and emplaced in Eocene volcano-sedimentary successions (including HIC) (Shafiei, 2010).

Moreover, these early preceding volcanics (including HIC) play a significant role in evolution of more evolved and more aqueous magma constructing Cu-Mo±Au porphyry deposits of KCMA, indicating a kind of maturation in arc magmatism.

According to Chiu et al. (2013), UDMA pre-collisional magmatism gradually have been ceased from north-west to south-east (from ca. 22 Ma in Meghri to ca. 6-10 Ma in Anar). This cessation is attributed to oblique and diachronous convergence between Arabia and Eurasia.

Hezar complex is one of the last phases of volcanism in Kerman Cenozoic Magmatic Arc (KCMA) (Dimitrijevic, 1973; Hassanzadeh, 1993).

2. ANALYTICAL METHODS

312 rock samples were collected, from which 190 were selected for detailed petrographical studies. Then, 40 samples were chosen for geochemical analysis taking into account the diversity of rock units and the location of the outcrops. These analyses were performed at SGS Co. (Australia and Canada branches) utilizing borate fusion XRF (code: GC XRF76V) for major elements and sodium peroxide fusion combined ICP-AES and ICP-MS (code: GE ICM90A) for trace elements.

For geochemical plots and calculations, GCDkit version 4.00 software and its R console with Microsoft Office Excel was utilized. For the age calculations, Isoplot 4 (Ludwig, 2012) has been used. The only change that has been made to the original settings of Isoplot is to adopt the new decay constant of ^{87}Rb, as presented by Villa et al. (2015). Ages calculated with this new decay constant are 2% older than the ages calculated with the decay constant of (Steiger and Jäger, 1977); so, for Cenozoic rocks, the difference is usually negligible.

The isotopic analyses (Sm-Nd and Rb-Sr) on seven samples were conducted in Isotope Geology Laboratory as a part of the Central Laboratory of Analyses of the University of Aveiro, Portugal. During the course of data gathering, replicates of the standards gave a mean value of $^{143}Nd/^{144}Nd$= 0.5121021± 50 (n = 17) for JNdi-1 and $^{87}Sr/^{86}Sr$ = 0.710261± 21 (n = 14) for SRM 987 which are used as standard values. The precisions on all isotopic ratios are given at 95% of confidence limit.

To calculate the $^{87}Rb/^{86}Sr$ and $^{147}Sm/^{144}Nd$ error, the following errors were assumed in providing concentrations: 10% for values less than 1 ppm, 5% for values less than 10 ppm and 2% for the remaining concentrations.

Errors on Nd and Sr isotopic compositions are <0.002% and errors on the $^{147}Sm/^{144}Nd$ ratio are predicted to be less than 0.1%. The initial Nd values at ca. 308 Ma were determined utilizing values of $^{147}Sm/^{144}Nd$ = 0.1967 (Jacobsen and Wasserburg, 1980) and $^{143}Nd/^{144}Nd$ = 0.512638 for the present-day chondritic uniform reservoir, CHUR (Wasserburg et al., 1981), and a ^{147}Sm decay constant of 6.54 × 10−12y−1 (Lugmair and Marti, 1978). TDM is computed with respect to the (DePaolo, 1981) mantle evolution model and also utilizing a linear evolution for a mantle separated from the CHUR at 4.55 Ga and having a present-day εNd value of +10 (TDM2). The whole rock oxygen isotope values were obtained at the Laboratory for Stable Isotope Science, University of Western Ontario, Canada. The procedure follows that of (Clayton and Mayeda, 1963) as modified by (Borthwick and Harmon, 1982) for use with ClF3. The accuracy is ±0.2‰ for homogenous samples and was checked by analyzing NBS-30, NBS-28, internal laboratory quartz, and kaolinite standard, respectively, both calibrated to their accepted values.

3. RESULTS

3.1. Field studies and Petrography

There are four different lithological units in the research location:

1) : Pyroclastic and volcano-sedimentary layers making the main part of the HIC. This unit comprises of welded and non-welded tuffs, and agglomerates, pyroclastic surges and volcanic breccia. Some of the tuffs demonstrate structures such as accretionary lapilli. Some evidence of flow structures can be observed in volcanic surges in which some fragments and clasts of the previous rocks are remained and confirm the currents'. The occurrence of agglomerate in the summit (4501m) may reveal that the current summit was not the summit or the vent at the time of extrusion. Because this agglomerate reveals that this place was at a lower height and was made because of a current flowing to this place. The later uplift of the summit may be the result of rising of the magma chamber which is obvious in Kamali.

   Pyroclastic rocks, as the most frequent lithologies all around the HIC, are exposed as diverse forms with different particle sizes. Most of these bodies are tuffs, although some coarse-grain lithologies such as lapilli tuff and agglomerate as lahar deposits and surge deposits exist. Crystal lithic tuff with flow imprints (as ignimbrite) is the most abundant type among tuffs. Further diversity in rock type has been recognized during this study especially in the southern flank of HIC.
2) : Lava flows which are interbedded with pyroclastic layers are not as widespread as them. These layers sometimes demonstrate columnar or prismatic structures in some parts of the southern flank of HIC around Ziarat village.
3) : Some bodies which make dikes, sills, and some rhyolite domes. These structures are geochronologically important due to their key role in dating the last phase of magmatism in this region. Among these units, Jalases (minor and major) are the most massive bodies. Minor Jalas and Major Jalas were both massive plugs and volcanic domes which have cut by a north-south

trending fault. Field investigations demonstrate that Jalas was apparently the place of the volcanic vent (or one of the vents) of HIC.

4) : Some plutonic bodies which have been raised along the southern fault. One of the most important instances of such bodies, Kamali, on the southern flank of the summit is made of gabbro and diorite.

Most of the HIC rocks are composed of pyroclastic welded rocks which have no analytical significance because of extensive alteration and mixing with other sedimentary materials. Lava rocks, on the other hand, are rare and widely weathered, altered and fractured with active faults of the region. Finding fresh samples within this active tectonic setting was an overwhelming task. Faulting with a northwest-southeast trend in the southern flank of HIC cause some intrusives such as Kamali and Jalas Minor and Major rise and crop out to the surface. Among the samples, Jalas dikes (samples number 16,23) intersected the Jalas Minor and Major are the last phases of magmatism in HIC (Table 1).

Then, the crystalline rocks studied geochemically including some (7 samples) selected for isotopic studies could be divided into three main categories according to their ages: 1): acidic to basic lava flows constructing the successions with pyroclastic material are the first volcanic materials extruded from the vent(s) (samples no. 08, 36 and 40) (Figure , a, b and h); 2): some intrusive bodies such as Kamali and Jalas Minor and Major cropping out of the southern flank of Hezar (sample no. 20) are then younger than the first category (Figure , e); 3): some acidic dikes cutting the Jalas Minor and Major are the last phases of magmatism in this region (samples no. 16 and 23) (Figure , f and g).

Whole Rock Geochemistry

The whole rock chemical compositions of Hezar rock units are shown in **Error! Reference source not found.**. Hezar Igneous Complex comprises of a wide variety of igneous rocks (basic, intermediate, and acid). As shown in Figure , despite the shoshonitic affinity (continental arc setting) that most of the previous works (Dimitrijevic, 1973; Hassanzadeh, 1993) and some more recent works had mentioned about the HIC, most of the studied samples lie in calc-alkaline domain (island arc setting). Although in some works on the north-western part of UDMA have been reported that calc-alkaline volcanism in early Oligocene gives way to a shoshonitic plutonism in late Oligocene.

Rock samples studied include the following types: 1): Volcanics: which could be grouped as a): Pyroclastics: which form the main part of the HIC. These rocks cover a wide diversity of the fall and flow materials such as tuff, volcanic breccia and agglomerate, volcano-sedimentary surge deposits; and b): Lava materials: which could be observed as sporadic volcanic layers between voluminous pyroclastic rocks and show a wide spectrum from basic to intermediate and even acid materials. 2): Plutonics: which were encountered in field research for the first time in this area and are limited to Kamali area (south-west of the summit). 3): Small intrusives: very rare materials which are spread over the limited parts as dikes and sills. This variety is symbolized and shown in the legend in Figure .

The major element composition of the studied rock samples are as follow: SiO_2 45-70% wt; TiO_2 0.1-1.7% wt; Al_2O_3 22-37% wt; Fe_2O_3t 1-12% wt; MgO 0.5-55% wt; CaO 2-11% wt; Na_2O 1.5-5% wt; K_2O 0.5-5.5% wt; P_2O_5 0.1-0.7% wt. But these compositional restrictions has demonstrated some differences between mafic and felsic (silicic) rocks. The mafic rocks show the following properties: TiO_2 > 1% wt; Fe_2O_3t > 8% wt; MgO > 3% wt; CaO> 8% wt; Na_2O < 3% wt; K_2O < 2.5% wt. Although these ranges in felsic (silicic) rocks are as follow: TiO_2 < 0.5% wt; Fe_2O_3t < 4% wt; MgO < 1.5% wt; 1.5< CaO < 8% wt; Na_2O > 3% wt; 6 > K_2O > 1.7% wt. The Mg number (Mg#=Mg/Mg+Fe) in felsic rocks (25-40) is evidently lower than that of mafic rocks (30-58). This may suggest that the felsic magma is more evolved (far from the mantle composition). This may be verified by low Cr content (<100 ppm) and low Ni content (<50 ppm). But this feature is evident in all samples (mafic and felsic).

In major element diagrams proposed by Irvine and Baragar (1971) and Miyashiro (1974) (not shown here), some samples (especially basic ones) show tholeiitic affinity. However, this affinity has not been verified by trace element diagrams (Winchester and Floyd, 1977; Pearce, 1983). It may be due to anhydrous fractionation which shifts the sample plots to higher FeO contents versus MgO, but it has no effect on the trace element signatures of the above diagrams. It may be the result of the mobility of the major elements due to a low-grade metamorphism. The differences between the domains of various diagrams of total-alkali versus silica by different authors (Cox, Bell and Pankhurst, 1979; Le Bas et al., 1986 ; Middlemost, 1994) can be interpreted by the same implication (Figure a).

Some of the emplacement processes for igneous rocks may be inferred by Harker diagrams of compatible and incompatible elements versus SiO_2 (not shown here) (Dampare et al., 2008). It seems that during the differentiation of ferro-magnesian minerals such as olivine and clinopyroxene, the concentration of compatible elements (Co, Cr, and Ni) decreases, however, the concentration of incompatible elements (Th, La, and Ba) increases. This effect is accompanied by a breaking point in SiO_2=55% or MgO=3% wt in most of these Harker diagrams. Low contents of Ni, Cr, and MgO may indicate some aspects of magma evolution. It seems that samples 9 and 33 are the nearest samples to primitive magma, because of their highest Ni (32 and 44 ppm), Cr (92 and 104 ppm), and MgO (5.52 and 5.02%) contents.

Harker diagrams of some major oxides vs. SiO_2 or MgO reveals the linear trends. This indicates that differentiation may be the main process in formation of these rocks. The contents of FeOt, MgO, and CaO decreases with an increase in SiO_2 content. The trend which is consistent with differentiation of earlier phases as olivine, pyroxene and plagioclase and participation of oxide minerals (magnetite and/or ilmenite) in the fractionating assemblage. A clear bending in Harker diagrams of MgO, TiO_2, and Cr may be associated with differentiating minerals from olivine to pyroxene. Then, crystallization conditions have promoted the growth of plagioclase crystals after reaching the SiO_2 content of magma to 55%.

It has been revealed that REE (specially LREE) can be mobile during hydrothermal alteration and low-grade metamorphism (Whitford et al., 1988). To make sure of the application of HFSE (especially REE) in the interpretation of tectonic setting and petrogenesis of the studied rocks, the diagrams of L.O.I versus Nb/La or Th/La can be used (Nude et al., 2015). Lack of correlation between L.O.I and these two ratios (diagrams not

shown) is compelling evidence that the concentration of Th, Nb, and LREE have not been disturbed in HIC. Then these elements can be used for evaluation of petrogenesis and tectonic setting of igneous rocks. Although inverse relation between L.O.I and SiO_2 along with low-to-medium content of L.O.I and the occurrence of quartz-calcite veins and epidote-chlorite in these rocks suggest low-grade metamorphism (Dampare et al., 2008). In the field and petrographic studies, it has been seen that in most samples, primary minerals partially or wholly altered to chlorite, epidote, and sericite; an observation which supports later hydrothermal alteration of these igneous rocks.

The ratio of $(La/Sm)_{PM}$ versus SiO_2 indicates that the pattern of normalized LREE to MREE is flatter in basic rocks and steeper in acid rocks because of the enrichment of LREE in the latter.

The extent of differentiation among different units have been estimated from the LREE/HREE ratio, which is demonstrated by the La/Yb ratio (between 4 to 8 in most of our samples). Besides, the LILE/HFSE ratio can be shown in Sr/Y. Differentiation trends of Sr-Yb (Figure c and d) have indicated the involvement of clinopyroxene and plagioclase minerals out of the stability domain of garnet, and apatite (Béguelin et al., 2015).

There are several REE model plots dealing with melting curves (lines) for spinel-lherzolite and garnet peridotite sources with depleted MORB mantle (DMM) and primitive mantle (PM) compositions. Different evidence supports enriched spinel lherzolite as the magma source of the HIC. The garnet lherzolite is rejected except sample no. 1. All samples are probably co-magmatic and have originated from a single depth that has been lower than the depth of sample no. 1 (Figure c and d).

The effects of fractional crystallization and crustal contamination

Th-Yb-Nb systems are very useful in determining both the source diversity and crustal assimilation in basic rocks because these elements as couples often are not dependent on fractional crystallization and/or partial melting (Nude et al., 2015; Pearce, 1983). Th/Yb versus Nb/Yb and TiO_2/Yb versus Nb/Yb are two brand new diagrams that have been developed using the last version by (Pearce et al., 2008). Th/Yb versus Nb/Yb diagram (Figure b) is developed for determining subduction-related settings and subduction-unrelated ones (Dilek and Furnes, 2011; Dilek and Furnes, 2014), though TiO_2/Yb versus Nb/Yb diagram (not shown) is used for systematics of the basaltic rocks independent to secondary alteration and enrichment processes related to subduction. Therefore, it can be used for determining the compositions of the primitive mantle source of the volcanic rocks (Pearce, 2008; Kasapoğlu et al., 2016).

4. DISCUSSION

In the diagram of Th/Yb versus Nb/Yb (Figure b**Error! Reference source not found.**) (Pearce, 2008), volcanic rocks lie out of the mantle array (MORB-OIB array) which may suggest the effect of crustal contamination or the flow of fluids in the subduction zone. Such contamination has increased the values of Th/Yb and has expelled the plot out of the mantle array. Evidently, our samples are higher than MORB-OIB array (or mantle array), suggesting that the source has subduction-related signatures. This is due to the input of Th from subduction-related fluids or magma to their sources. The contamination of oceanic basalts with subducted sediments, oceanic crust and/or recycling crust, all can cause this displacement (Pease et al., 2016). Additionally, the magmatic evolution series, parallel to MORB-OIB array, can be because of the influence of fractional crystallization. It should be stated that all samples have Nb/Yb ratios more than 1.0, recommending an active continental margin as a source and rejecting an oceanic arc system.

In TiO_2/Yb versus Nb/Yb diagram (not shown but similar to Figure b), most of our basic samples concentrate around the transition line between E-MORB and N-MORB, although more evolved rocks show a trend to lower TiO_2/Yb values and higher Nb/Yb values, suggesting the effects of magmatic differentiation (probably due to elimination of TiO_2–bearing phases). This diagram can be used for determining the melting depth and then mantle temperature and thickness of the lithosphere during magma generation (Pease et al., 2016). Lower TiO_2/Yb values in our samples (MORB-OIB array), indicate lower depth (and formation temperature) compared with OIB.

All of the samples of HIC, fall in a field in $(Nb/Th)_{PM}$ vs. $(Nb/La)_{PM}$ diagram that suggest crustal contamination or input of the solutions from the subducted slab. Higher values of normalized Th and La content, shown by lower values of $(Nb/Th)_{PM}$ and $(Nb/La)_{PM}$, suggest higher degrees of crustal contamination.

As it is evident in Figure d, in most of the samples Eu/Eu* index (Eu/Eu* = (2Eu/Eu chondrite)/ (Sm/Sm chondrite + Gd/Gd chondrite)) lie between 0.8-1.1. Lack of Eu anomaly in most of the samples (except only two samples) indicates that there is no sign supporting differentiation or otherwise settlement of plagioclase and/or K feldspar in the magma chamber.

Magma and melting characteristics can be investigated through REE modeling.

Emplacement and tectonic setting

Immobile elements and their ratios can be used for determination of tectonic setting of the rocks studied. To achieve this goal, several discriminating diagrams should be used (Nude et al., 2015). Many diagrams have been developed by different authors interpreting the tectonic setting of rock assemblages using major and trace elements. Major elements are still used in this kind of interpretations because of their simple application. But their mobility imposes some doubts about their usage in older altered or metamorphosed terrains (Verma, 2010). Then, some diagrams are set aside in this study (Pearce , Gorman and Birkett, 1977; Shervais, 1982).

Using diagrams based on major elements (Figure c) such as (Mullen, 1983; Verma, Guevara and Agrawal, 2006) is of concern in older terrains, because major elements may have different behaviors during alteration or metamorphism. Then, it is recommended that the results shown by these diagrams be rechecked using diagrams prepared with trace elements (Agrawal, Guevara and Verma, 2008; Wood, 1980).

As it is evident in Figure a, all of the studied rock samples of HIC lie in the field of calc-alkaline and island arc basalts, i.e. destructive plate margin basalts and their differentiates. In triangular plots of (Wood, 1980) (Figure a), one sample lies outside of CAB field. It may occur because Ta acts like Ti in the

differentiation of ferromagnesian and Fe minerals. Then, this sample may come close to the Ta apex, due to this differentiation. It should be noted that the border between IAT and CAB in D domain is not accepted by IUGS nomenclature recommendations, and these two domains are considered as a single domain, i.e. IAB.

The multiple diagrams (one of which is shown in Figure b) are more accurate because of multiple checking the geochemical conditions with tectonic settings. Evidently, log- ratios of major elements (Verma, Guevara and Agrawal, 2006) and trace elements (Agrawal, Guevara and Verma, 2008) have shown the same results.

Spider diagram (Figure) is another tool for interpreting the magmatic evolution of igneous rocks and their emplacement and tectonic setting. The parallel patterns in all of the following diagrams may indicate the comagmatic character of the studied rocks. Magma rising through a thick continental crust may be the source of crustal contamination, which has led to higher Rb/Sr and LILE/HFSE and has increased the Th content as a result of AFC processes (Tamura et al., 2011).

The negative anomaly of Ti and Nb may indicate magmatic relation with subduction (e.g. calc-alkaline volcanic arc of continental active margin). This can be due to earlier depletion events in the mantle source. Two other minimum points, i.e. Ti and P, may be due to early crystallization of titano-magmetite and ilmenite and fractional crystallization of apatite, respectively. The concentration of incompatible elements, especially REEs and LILEs, standardized with primitive mantle shows enrichment of magma in Rb, Ba, K, and Th. The above trends are pieces of evidence supporting that the HIC magma is contaminated with materials from the deep continental crust. At the same time, magma was mixed with volatiles rich in early-melting components of oceanic crust. Lack of Sr and Eu anomaly in most of the rock samples may prove lack of fractional crystallization of plagioclase in the magmatic melt. Enrichment of LREE quantified as La/Sm ratio- and Eu anomaly, indicate higher degrees of REE differentiation. MREE to HREE are flat. Then there is no sign of garnet or spinel as the refractory phase during the melting. These conditions which are observed in few samples are because of eliminating plagioclase from the source or later, through fractional crystallization in the magma chamber before emplacement.

The troughs of Ti, Nb, and Ta are usual in calc-alkaline magma and may be explained by the remained hornblende and Fe-Ti oxides in the source of parental magma (Pearce and Norry, 1979). Both of Nb and Ta are very incompatible with typical mantle associations and are inactive during metasomatic events. Then their anomalies can be described with adding slab elements from the dehydrated oceanic crust into the mantle wedge, by which several incompatible elements – except Nb- are increased (Turner et al., 2003; Wang et al., 2006). All of the samples demonstrate the same patterns in incompatible elements- i.e. they relatively have been enriched in highly-mobile elements (LILE) and have been depleted in immobile elements (HFSE).

Rb-Sr and Sm-Nd Isotopic Data

Isotopic analyses for Rb/Sr and Sm/Nd systems for seven samples, which are introduced in Table 1, are shown in Table 2.

Epsilon Nd values are always positive which indicate that the rocks solidified from magmas that evolved (probably through fractional crystallization) from parental melts generated in the mantle with no (or only small) assimilation of crustal rocks (Figure). However, there are some variations in those values (between +3.4 and +0.3, for 40 Ma), indicating either participation of different mantle sources or variation in the degree of crustal assimilation (although, in this hypothesis, it should be always small, because epsilon Nd is always positive).

$^{87}Sr/^{86}Sr$ (and consequently epsilon Sr) values in most samples are relatively high (Figure and Figure), taking into account the positive epsilon Nd values. In fact, only S53 and S60 plot close to the so-called "mantle array". Some displacement to the right is expected in magmas whose sources are located in mantle wedges above the subduction zone. However, the displacement of the remaining five samples, in particular of S51 ($^{87}Sr/^{86}Sr$ = 0.70663, for 40 Ma; $^{87}Sr/^{86}Sr$= 0.70658, for 50 Ma), suggests that they probably underwent a post-magmatic increase of the $^{87}Sr/^{86}Sr$ ratio by crustal fluids, which typically occurs during hydrothermal alteration. In fact, alteration commonly disturbs the $^{87}Sr/^{86}Sr$ ratio without affecting the $^{143}Nd/^{144}Nd$ ratio because Sr is much more soluble than Nd in aqueous fluids. Therefore, whilst epsilon Nd values are preserving the original signatures of the igneous processes, the $^{87}Sr/^{86}Sr$ ratios (and epsilon Sr values) may represent a superimposition of two signatures. At least S51 (but also probably some of the other samples) should have suffered important hydrothermal alteration.

Sr-Nd Geochronology

All of the magmatic features in Urumieh-Dokhtar are of pre-collisional features which have been ceased in 22 Ma except for some limited post-collisional features mainly in Armania and the north-western part which have been initiated about 11 Ma (Chiu et al., 2013).

Two phases of magmatism in KCMA are defined: the first phase is initiated with early Eocene volcanic series (Bahraseman Complex) which continues to middle-upper Eocene (Razak Complex) (Dimitrijevic et al., 1973; Hassanzadeh, 1993). These volcanic rocks show a transition from tholeiitic to calk-alkaline series indicating the tectonic setting of island arcs. This island arc volcanism was followed by a plutonic activity during Oligocene (Jebal Barez granitoids). The magmatism is continued into mid-Oligocene to Hezar volcanic complex (the subject of this study) which is mainly attributed to shoshonitic rocks with arc-continent magma properties (Dimitrijevic et al., 1973; Hassanzadeh, 1993), but as it was mentioned before, according to our study this part lies in calc-alkaline affinity with island arc characteristics.

The second phase (the plutonic activity) is initiated in mid-Miocene. The representative of this intrusive is shallow porphyry granitoid stocks (Kuh Panj granitoids) with adakitic signatures (Dimitrijevic et al., 1973). Shallow intrusive activity continues to late Miocene and Pliocene in a post-collisional tectonic setting which has made subvolcanic bodies (Dehaj type), two single stratovolcano (Mosahem type), and some cones (Aj type) (Dimitrijevic et al., 1973; Hassanzadeh, 1993).

In seven samples selected for isotopic analysis and geochronological interpretations, because of limitations in the number of samples, it was attempted to gather as many variations as possible: two samples from Jalas Minor (S60) and Jalas Major (S53) are subvolcanic (Jalas dikes) which are the last phases of volcanism in this region. As it is evident in Figure , these two chemically different samples are the nearest

samples to "mantle array". Two samples are selected from one acidic intrusive in the southern flank (S51) and an andesitic lava flow in the westernmost part of the HIC in Mirshadi Valley (S73) hoping that has a relationship with other parts. But these are the extreme data that cannot be used in the geochronological analysis. Three other samples (S45, S77, and S57) are selected from the main part of the HIC (Table 1). Their place in Figure indicates their relation.

Obtaining an isochron using all of these data is difficult since the range of $^{87}Rb/^{86}Sr$ is very small (0.114 to 0.998). In fact, it was confirmed that there is no Rb-Sr isochron, unless we consider only samples S45, S57, and S77 (as it is explained in the previous paragraph). In this case, the result is an age of 47 ± 5 Ma, with MSWD = 0.44 (Figure).

Using samples S53 and S60, an "age" of 6.4 ± 2.6 Ma is obtained. However, this is not really an isochron because it is calculated based on a straight line obtained with only two points. As it is mentioned previously, these two samples from Jalas Minor and Major are of two dikes which are the last phases of volcanism in this region (Figure g). Because Jalas Mountain cut through the main part of the HIC and these subvolcanics cut the Jalas body. Also, as it is clear in Figure these two chemically different samples are the nearest samples to "mantle array".

With the Sm-Nd system typically it is even more difficult to obtain whole-rock isochrons because most of the rocks show a very small variation of the $^{147}Sm/^{144}Nd$ ratio. $^{87}Rb/^{86}Sr$ varies from 0.114 to 0.988 (the largest value is nine times greater than the smallest) whilst $^{147}Sm/^{144}Nd$ varies only from 0.101 to 0.151 (the largest value is only one and a half times greater than the smallest). If the ranges of $^{147}Sm/^{144}Nd$ ratios were similar to the ranges of $^{87}Rb/^{86}Sr$ ratios, the Sm-Nd system would be a much powerful way of getting reliable ages because Sm and Nd are much less affected by alteration than Rb and Sr. Then Rb/Sr system analysis gives more accurate ages than Sm/Nd system analyses.

5. CONCLUSIONS

Hezar Igneous Complex (HIC) is originated by the intersection of north-south Sabzevaran fault and NW-SE Rafsanjan-Rayen fault. It is demonstrated that the possible place of the conduit and vent is in Jalas Mountain which has been split later by the first fault of the above faults into Minor and Major Jalas. The current summit had been arisen by ascending magma chamber under the HIC that constitutes the Kamali Mountain at the south of the summit. The evidence of plutonic rocks of the HIC is exposed in Kamali Mountain. The sub-alkaline rocks of this complex mainly are made of different pyroclastic and lava rocks, acidic to basic revealing the evidence of fractional crystallization and mineral segregation. The evidence of sequential explosive and effusive eruptions with Strombolian to Vulcanian types is obvious. The compositional trend of the rocks is more associated with the melting of spinel lherzolite, not garnet lherzolite. The subduction-related mechanism of the magma genesis has been demonstrated by the IAB nature of the magma formation in geochemical diagrams. It seems that the later movement of the southern fault, i.e. Rafsanjan- Rayen fault, has devastated the southern part of the HIC comprising of its main vent in Jalas and has made a suitable place for ascending the lower plutonic rocks, exposed in Kamali Mountain.

Positive εNd values indicate that the rocks solidified from evolved magmas (probably through fractional crystallization) from different parental melts generated in the mantle with no (or only small) assimilation of crustal rocks. Some displacement to the right of the "mantle array" is due to their origin from mantle wedges above the subduction zone. Alteration disturbed $^{87}Sr/^{86}Sr$ ratios without affecting $^{143}Nd/^{144}Nd$ ratios.

Drawing an Rb-Sr isochron in three related samples resulted in an age of 44± 5 Ma for HIC main edifice, which is cut by Jalas intrusive body, that in turn cut by some dikes giving an ambiguous age of 6.4 Ma.

6. ACKNOWLEDGMENTS

This study was carried out through Ph.D. thesis of the first author at Shahid Bahonar University of Kerman, Iran. Part of the costs of whole-rock geochemical analyses was provided through a research grant by IMIDRO (Iranian Mines & Mining Industries Development & Renovation). Whole-rock analyses were performed in SGS laboratories in Australia and Canada. Isotopic and dating analyses were carried out in Laboratory of Isotope Geology (Laboratório de Geologia Isotópica) of the University of Aveiro (Universidade de Aveiro), Portugal (LGI-UA). Abbas Hosseinipour, Ali Alirezaei, Masoud Moghaddas, Hassan Sadeghi, Ali Shahabi, Ali Naghdi, and Mahmoud Rahjou took part in field works. Some of the tools and materials needed, prepared by Ahad Soltani from Keele University, UK, Saeid Aghaei and Dr. Ahmad Abbasnejad. Technical and Vocational University of Iran, specially Hatam Salimi (former president of Shahid Chamran Technical College) and Mohsen Lotfi (head of Neyshabur Technical College) are acknowledged for their official assistance with the first author. Finally, we want to thank warmly all guidance and points of view from Dr. Mohammad Hashem Emami, Dr. Mohsen Arvin, and Dr. Sara Dargahi.

REFERENCES

1. Agrawal S, Guevara M, Verma SP. Tectonic discrimination of basic and ultrabasic volcanic rocks through log-transformed ratios of immobile trace elements. Int Geol Rev. 50 ،1057–1079 (2008)
2. Aldanmaz E, Pearce JA, Thirlwall M, Mitchell J. Petrogenetic evolution of late Cenozoic, post-collision volcanism in western Anatolia, Turkey. J Volcanol Geotherm Res., 102 ،67–95 (2000)
3. Alimohammadi, M., Alirezaei, S., Kontak, DJ. Application of ASTER data for exploration of porphyry copper deposits: A case study of Daraloo–Sarmeshk area, southern part of the Kerman copper belt, Iran. Ore Geol. Rev. 70, 290–304 (2015). doi:10.1016/j.oregeorev.2015.04.010
4. Béguelin P, Chiaradia M, Beate B, Spikings R. The Yanaurcu volcano (Western Cordillera, Ecuador): A field, petrographic, geochemical, isotopic and geochronological study. Lithos. 218 ،37–53 (2015)

5. Berberian M, King GC. Towards a palaeogeography and tectonic evolution of Iran. (1981).
6. Borthwick J, Harmon RS. A note regarding CIF3 as an alternative to BrF5 for oxygen isotope analysis. Geochim Cosmochim Acta. 46 ،1665–1668 (1982)
7. Chiu H-Y, Chung S-L, Zarrinkoub MH, Mohammadi SS, Khatib MM, Iizuka Y. Zircon U–Pb age constraints from Iran on the magmatic evolution related to Neotethyan subduction and Zagros orogeny. Lithos [Internet]. 162-163, 70-87. (2013) Available from: http://www.sciencedirect.com/science/article/pii/S002449371300011X
8. Clayton RN, Mayeda TK. The use of bromine pentafluoride in the extraction of oxygen from oxides and silicates for isotopic analysis. Geochim Cosmochim Acta. 27 ،43–52 (1963)
9. Cox KJ, Bell, JD, Pankhurst RJ. The Interpretation of Igneous Rocks. St Leonards, NSW, Australia.: Allen and Unwin 450 .(1979)
10. Dampare S, Shibata T, Asiedu D, Osae S, Banoeng-Yakubo B. Geochemistry of Paleoproterozoic metavolcanic rocks from the southern Ashanti volcanic belt, Ghana: petrogenetic and tectonic setting implications. Precambrian Res. 162 ،403–423 (2008)
11. Dayani Tilaki MS, Alidadi H, Taghipour A, Yazdani M, Teimori GH, Choupani A, Navaei AA. Evaluation of noise pressure level at mosques at the time of religious ceremonies. J Adv Pharm Edu Res, 8(1), 13-16 (2018).
12. DePaolo DJ. Trace element and isotopic effects of combined wallrock assimilation and fractional crystallization. Earth Planet Sci Lett. 53 ،189–202 (1981)
13. Dilek Y, Furnes H. Ophiolite genesis and global tectonics: geochemical and tectonic fingerprinting of ancient oceanic lithosphere. Geol Soc Am Bull. 123 ،387–411 (2011)
14. Dilek Y, Furnes H. Ophiolites and their origins. Elements. 10 ،93–100 (2014)
15. Dimitrijevic MD. Geology of Kerman Region. Geological Survey of Iran .Report No.: YU. 59 (1973).
16. Hassanzadeh J. Metallogenic and tectonomagmatic events in the SE sector of the Cenozoic active continental margin of central Iran (Shahr e Babak area, Kerman Province) [Ph.D. dissertation]. [Los Angeles]: University of California; (1993)
17. Irvine Tn, Baragar Wra. A guide to the chemical classification of the common volcanic rocks. Can J Earth Sci. 8 ،523–548 (1971)
18. Jacobsen SB, Wasserburg G. Sm-Nd isotopic evolution of chondrites. Earth Planet Sci Lett.; 50: 139-155 (1980)
19. Kananian A, Sarjoughian F, Nadimi A, Ahmadian J, Ling W. Geochemical characteristics of the Kuh-e Dom intrusion, Urumieh–Dokhtar Magmatic Arc (Iran): Implications for source regions and magmatic evolution. J Asian Earth Sci [Internet]. 90:137–148 (2014). Available from: http://linkinghub.elsevier.com/retrieve/pii/S1367912014001977
20. Kasapoğlu B, Ersoy YE, Uysal İ, Palmer MR, Zack T, Koralay EO, et al. The Petrology of Paleogene Volcanism in the Central Sakarya, Nallıhan Region: Implications for the Initiation and Evolution of Post-Collisional, Slab Break-off Related Magmatic Activity. Lithos. (2016)
21. Le Bas MJ, Le Maitre R, Streckeisen A, Zanettin B, others. A chemical classification of volcanic rocks based on the total alkali-silica diagram. J Petrol. 27 ،745–750 (1986)
22. Ludwig K. Isoplot 3.75: A Geochronological Toolkit for Microsoft Excel: Berkeley Geochronology Center Special Publication 5, p. 75 (2012).
23. Lugmair G, Marti K. Lunar initial 143Nd/144Nd: differential evolution of the lunar crust and mantle. Earth Planet Sci Lett. 39 ،349–357 (1978)
24. McKenzie D, O'nions R. Partial melt distributions from inversion of rare earth element concentrations. J Petrol. 32 ،1021–1091 (1991)
25. Middlemost EA. Naming materials in the magma/igneous rock system. Earth-Sci Rev. 37 ،215–224 (1994)
26. Miyashiro A. Volcanic rock series in island arcs and active continental margins. Am J Sci. 274 ،321–355 (1974)
27. Moshfe A, Kohansal MA, Parhizgari N, Khoramrooz SS, Abbasi M, Niyyati M, Akbarzadeh A, Jamshidi A. A review: isolation of acanthamoeba species in surface waters of yasuj district south of Iran. Pharmacophore, 8(2), 39-43 (2017).
28. Mullen ED. MnO/TiO 2/P 2 O 5: a minor element discriminant for basaltic rocks of oceanic environments and its implications for petrogenesis. Earth Planet Sci Lett. 62 ،53–62 (1983)
29. Nakamura N. Determination of REE, Ba, Fe, Mg, Na and K in carbonaceous and ordinary chondrites. Geochim Cosmochim Acta. 38 ،757–775 (1974)
30. Niktabar S., Moradian A, Ahmadipour H, Santos JF, Mendes MH. Petrogenesis of Lalehzar granitoid intrusions (Kerman Province- Iran). J Sci. Unpublished Accepted paper (2016)
31. Noorizadeh M, Moradian A, Ahamadipour H, Ghassemi MR, Santos JF. Petrology, Geochemistry and Tectonomagmatic Evolution of Hezar Igneous Complex (Rayen- South of Kerman- Iran): the First Description of an Arc Remnant of the Neotethyan Subduction Zone. J. Sci. 29 (4): 341-359 (2018).
32. Noorizadeh M, Moradian A, Ahmadipour H, Ghassemi MR. Analysis of Geotourism Strategies in Rayen- Kerman Using SWOT method. In: The 2nd National Conference on Iranian Tourism and Ecotourism. Hamedan; (2013).
33. Nude PM, Kwayisi D, Taki NA, Kutu JM, Anani CY, Banoeng-Yakubo B, et al. Petrography and chemical evidence for multi-stage emplacement of western Buem volcanic rocks in the Dahomeyide orogenic belt, southeastern Ghana, West Africa. J Afr Earth Sci 112, Part A:314–327 (2015). Available from: http://www.sciencedirect.com/science/article/pii/S1464343X15300716
34. Pearce JA, Norry MJ. Petrogenetic implications of Ti, Zr, Y, and Nb variations in volcanic rocks. Contrib Mineral Petrol. 69 ،33–47 (1979)
35. Pearce JA. Geochemical fingerprinting of oceanic basalts with applications to ophiolite classification and the search for Archean oceanic crust. Lithos. 100 ،14–48 (2008)

36. Pearce JA. Role of the sub-continental lithosphere in magma genesis at active continental margins. (1983)
37. Pearce T, Gorman B, Birkett T. The relationship between major element chemistry and tectonic environment of basic and intermediate volcanic rocks. Earth Planet Sci Lett. 36 ‹121–132 (1977)
38. Pease V, Scarrow J, Silva IN, Cambeses A. Devonian magmatism in the Timan Range, Arctic Russia—subduction, post-orogenic extension, or rifting? Tectonophysics. (2016)
39. Peters TJ, Menzies M, Thirlwall M, Kyle PR. Zuni–Bandera volcanism, Rio Grande, USA—Melt formation in garnet-and spinel-facies mantle straddling the asthenosphere–lithosphere boundary. Lithos. 102 ‹295–315 (2008)
40. Shafiei B. Lead isotope signatures of the igneous rocks and porphyry copper deposits from the Kerman Cenozoic magmatic arc (SE Iran), and their magmatic-metallogenetic implications. Ore Geol Rev [Internet]; 38:27-36 (2010) Available from: http://www.sciencedirect.com/science/article/pii/S0169136810000570
41. Shervais JW. Ti-V plots and the petrogenesis of modern and ophiolitic lavas. Earth Planet Sci Lett. 59 ‹101–118 (1982)
42. Steiger R, Jäger E. Subcommission on geochronology: convention on the use of decay constants in geo-and cosmochronology. Earth Planet Sci Lett. 36:359-362, (1977).
43. Sun S-S, McDonough W. Chemical and isotopic systematics of oceanic basalts: implications for mantle composition and processes. Geol Soc Lond Spec Publ. 313(1), 42-45 (1989)
44. Suvorov OA, Kuznetsov AL, Shank MA, Volozhaninova SY, Pugachev IO, Pasko OV, Babin YV. Electrochemical and Electrostatic Decomposition Technologies As A Means of Improving the Efficiency and Safety of Agricultural and Water Technologies. Int.J. Pharm. Res. Allied Sci., 7(2), 43-52 (2018).
45. Tamura Y, Ishizuka O, Stern R, Shukuno H, Kawabata H, Embley R, et al. Two primary basalt magma types from northwest Rota-1 volcano, Mariana arc and its mantle diapir or mantle wedge plume. J Petrol. egr022 (2011)
46. TURNER S, FODEN J, GEORGE R, EVANS P, VARNE R, Elburg M, et al. Rates and processes of potassic magma evolution beneath Sangeang Api volcano, East Sunda arc, Indonesia. J Petrol. 44 ‹491–515 (2003)
47. Verma SP, Guevara M, Agrawal S. Discriminating four tectonic settings: Five new geochemical diagrams for basic and ultrabasic volcanic rocks based on log—ratio transformation of major-element data. J Earth Syst Sci. 115 ‹485–528 (2006)
48. Verma SP. Statistical evaluation of bivariate, ternary and discriminant function tectonomagmatic discrimination diagrams. Turk J Earth Sci. 19 ‹185–238 (2010)
49. Wang F, Peng Z, Zhu R, He H, Yang L. Petrogenesis and magma residence time of lavas from Tengchong volcanic field (China): evidence from U series disequilibria and 40Ar/39Ar dating. Geochem Geophys Geosystems. 7 (1) (2006)
50. Wasserburg G, Jacobsen S, DePaolo D, McCulloch M, Wen T. Precise determination of SmNd ratios, Sm and Nd isotopic abundances in standard solutions. Geochim Cosmochim Acta.; 45 2311-2323 (1981).
51. Whitford D, Korsch M, Porritt P, Craven S. Rare-earth element mobility around the volcanogenic polymentallic massive sulfide deposit at Que River, Tasmania, Australia. Chem Geol. 68 ‹105–119 (1988)
52. Winchester J, Floyd P. Geochemical discrimination of different magma series and their differentiation products using immobile elements. Chem Geol. 20 ‹325–343 (1977)
53. Wood DA. The application of a Th Hf Ta diagram to problems of tectonomagmatic classification and to establishing the nature of crustal contamination of basaltic lavas of the British Tertiary Volcanic Province. Earth Planet Sci Lett. 50 ‹11–30 (1980).

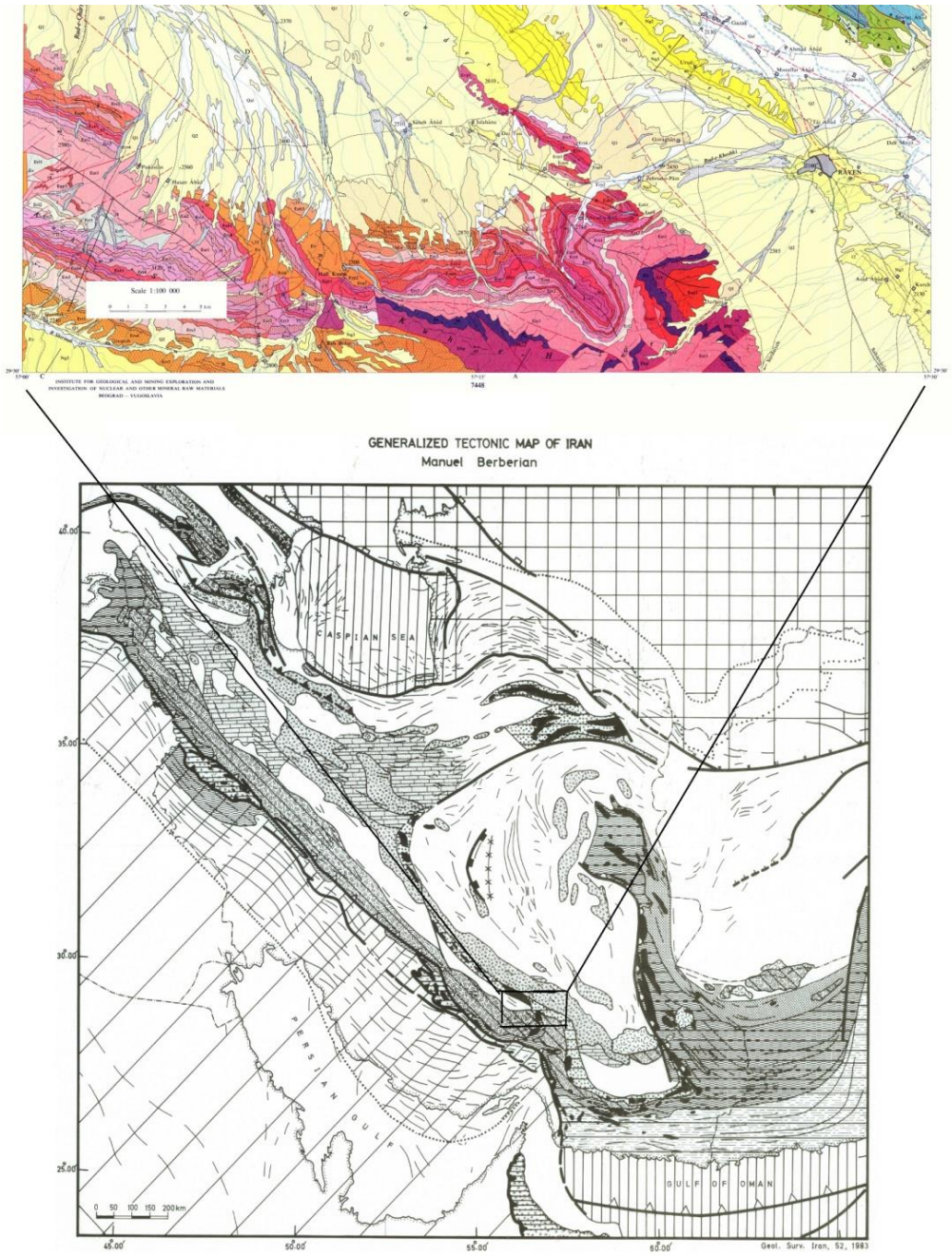

Figure 1- Lower map: The approximate location of the studied area in the structural map of Iran (out of scale) (Berberian and King, 1981). Upper map: South-western part of 1/100.000 geological map of Rayen- Kerman, showing the volcano-sedimentary successions of Hezar Igneous Complex (Dimitrijevic et al., 1973). The scale included.

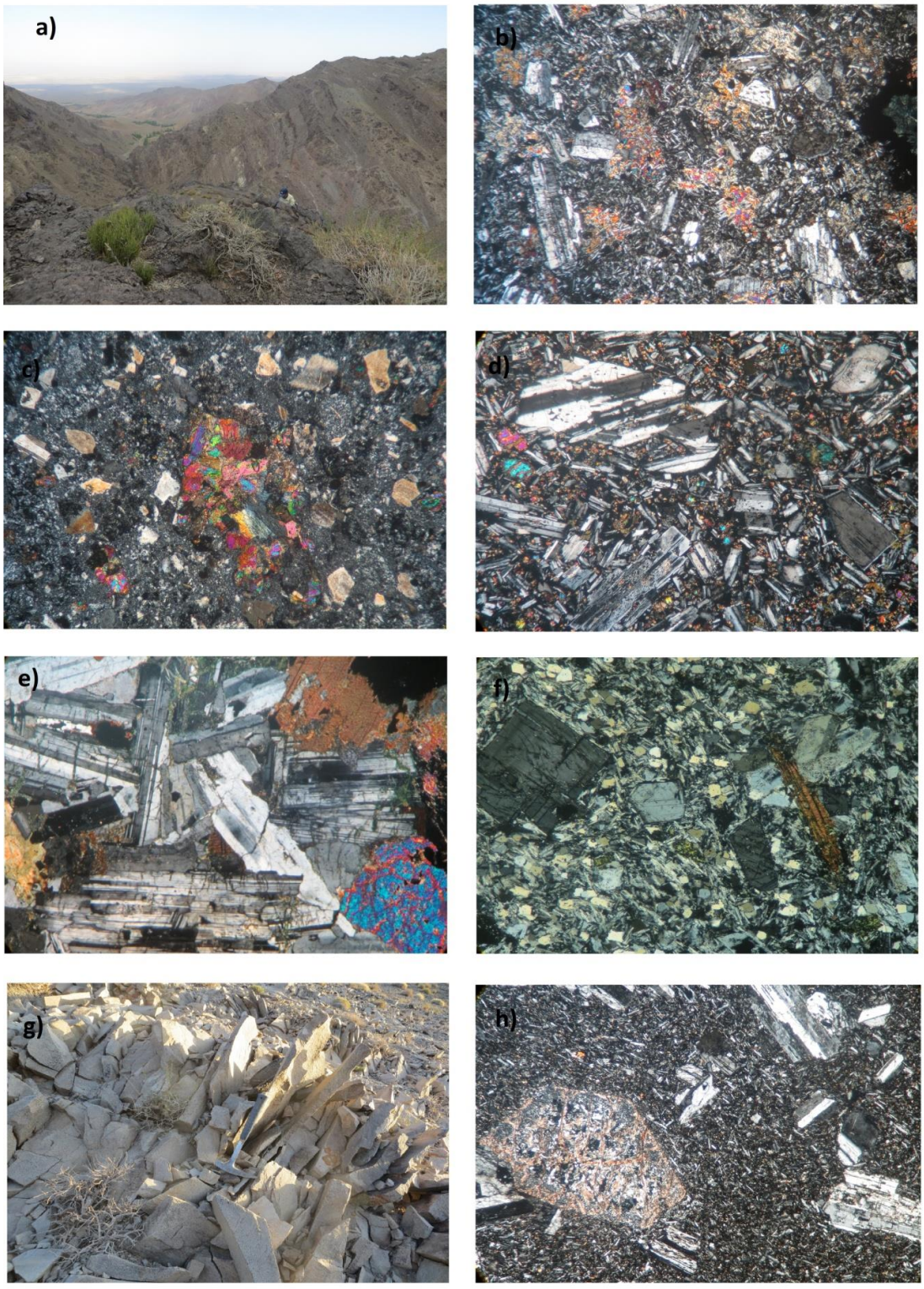

Figure 2- The petrographic properties and field features for some of the rock samples. a) successions of pyroclastic and lava materials in Babini Valley, the eastern part of the complex; b), c) and d) different microscopic textures of the succession of a). Altered samples shown in b, and d. And c. is unaltered andesite. ; e) Gabbro from Kamali. Pyroxene is replaced with secondary minerals such as chlorite, epidote and Fe oxides; f) rhyolitic intrusions in Minor Jalas under the microscope; g) rhyolite with the columnar structure in Minor Jalas; h) trachitic texture in basalt.

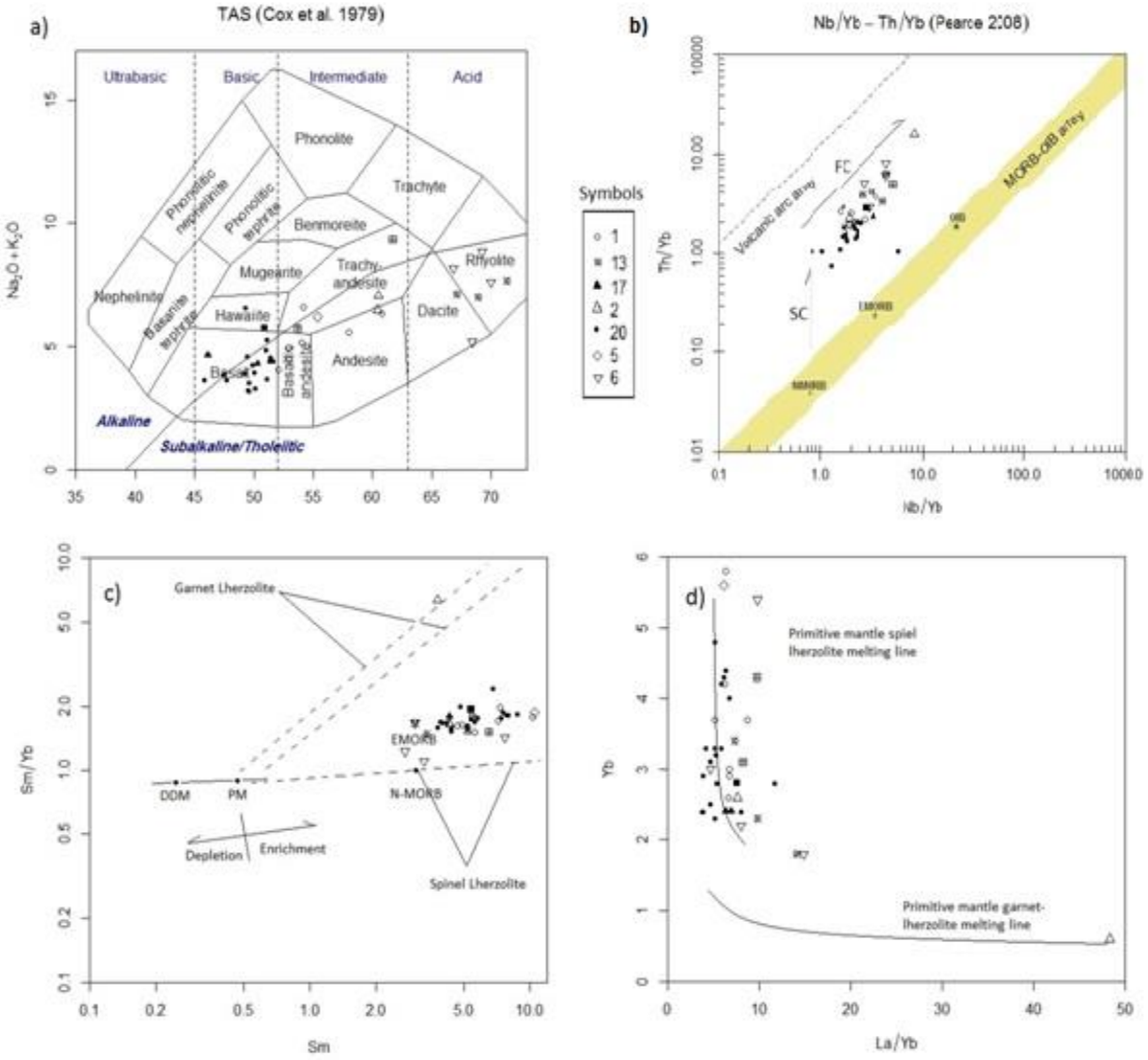

Figure 3- a) Total alkali versus silica plot showing the chemical classification of volcanic and subvolcanic rocks of HIC (Cox, Bell and Pankhurst, 1979); b) Th/Yb vs. Nb/Yb discriminating MORB-OIB array from volcanic arc array (Pearce, 2008); c) REE model plot of Sm/Yb vs. Sm for HIC samples (Aldanmaz et al., 2000; Nude et al., 2015). The heavy line represents the mantle array defined by DMM (McKenzie and O'nions, 1991) and PM (Sun S-S, McDonough, 1989) compositions. The N-MORB and E-MORB compositions (Sun S-S, McDonough, 1989) have also been shown; d) REE model plot of Yb vs. La/Yb for HIC samples (Peters et al., 2008) from (Niktabar et al., 2016). The symbols used in geochemical diagrams and plots: 1) Intermediate lava; 2) Intermediate subvolcanics; 5) Pyroclastics; 6) Acid dikes; 13) Acid lava; 17) Basic subvolcanics; 20) Basic lava.

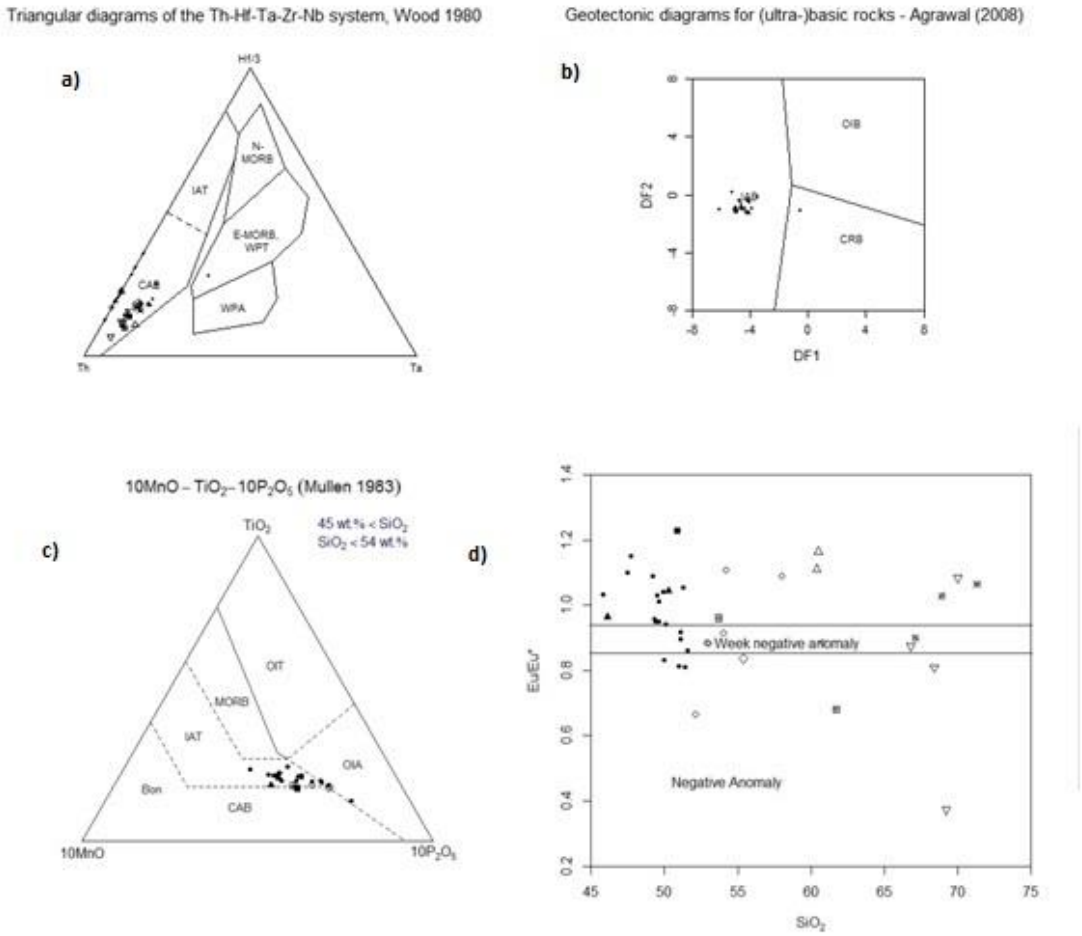

Figure 4- a) Ternary diagrams discriminating tectonic settings. The other triangular diagrams have been omitted due to their similarities. The samples lie in the realm of calc-alkaline basalts; b) Geotectonic diagram for basic rocks using trace elements. Other four diagrams are omitted because of their similarities (Agrawal , Guevara and Verma, 2008); c) Ternary diagram of MnO- TiO_2-P2O5 (Mullen, 1983). Nearly all samples lie in the field of Island Arc Tholeiite (or Basalt); d) Negative Eu anomaly in some samples may indicate fractional crystallization of plagioclase in the magma chamber.

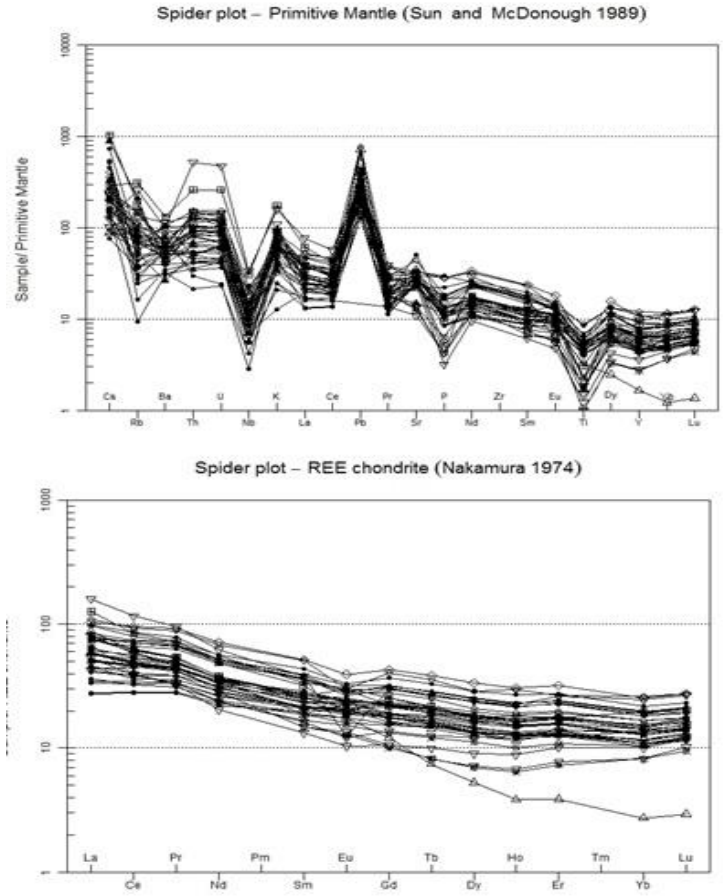

Figure 5- a) The spider plot of elemental values of HIC samples normalized with primitive mantle (Sun S-S, McDonough, 1989); b) The spider plot of REE values of HIC samples normalized with chondrite (Nakamura et al., 1974).

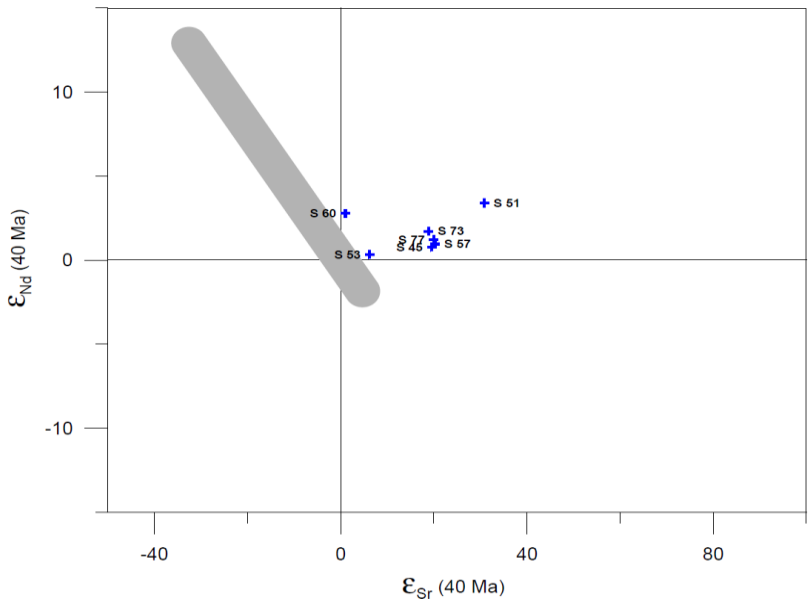

Figure 6- εNd vs. εSr calculated for 40 Ma in seven samples. Positive epsilon Nd values indicate a mantle source without much engagement of crustal materials.

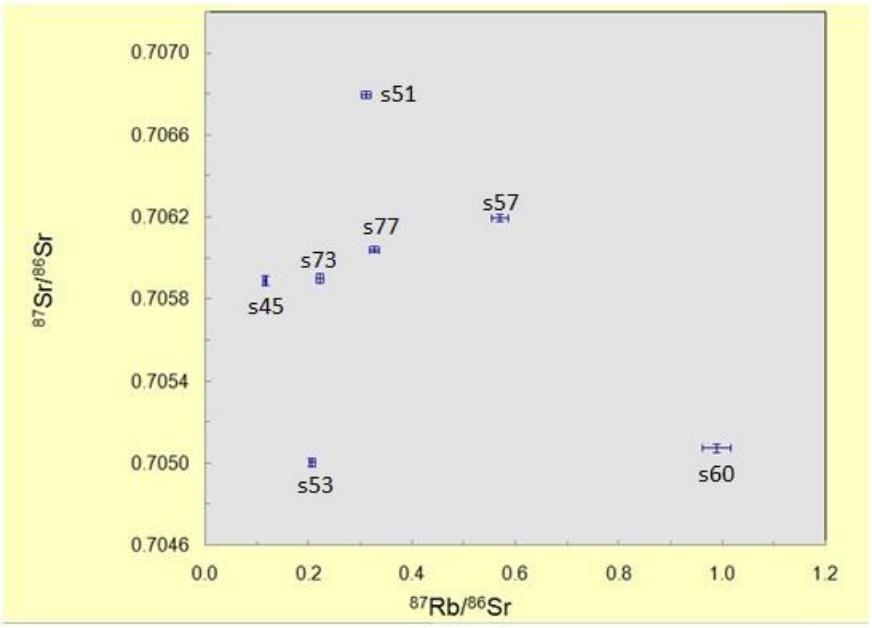

Figure 7- Relation between the ratio of $^{87}Sr/^{86}Sr$ versus $^{87}Rb/^{86}Sr$ in seven samples.

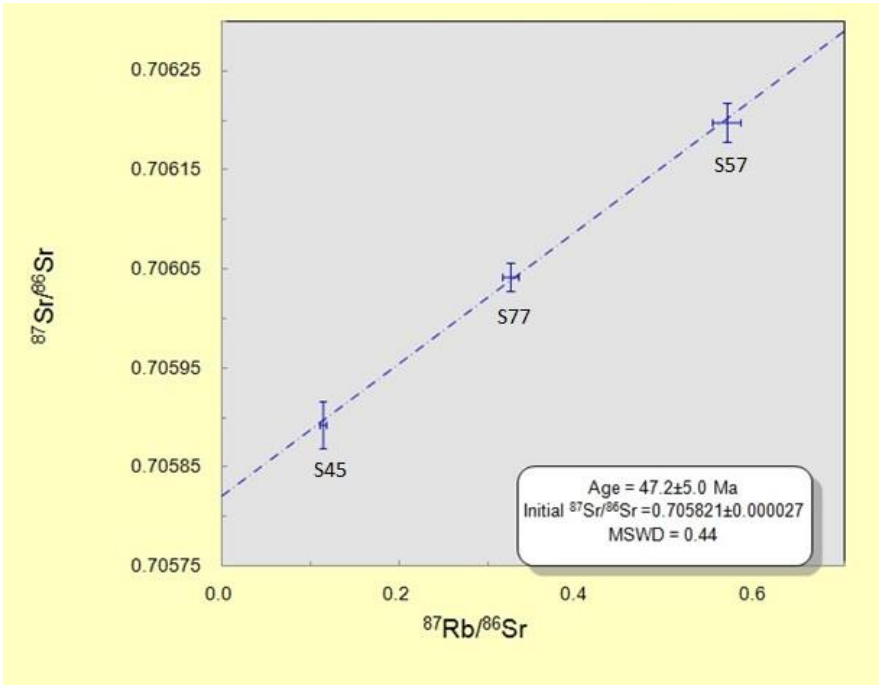

Figure 8- Isochron of three samples (S45, S57, S77) showing Mean Square Weighted Deviation (MSWD) and initial value of $^{87}Sr/^{86}Sr$.

Table 1- Seven samples used for isotopic analyses have different field characteristics. **Error! Reference source not found.**Samples from the main body of the Hezar edifice used for constructing the isochron number 1 and the subvolcanic materials used for constructing the isochron number 2. The sample number 14 – the farthest sample from the center of the HIC- has no relation with these two isochrons, which is eliminated from the calculations. Sample number 20 – from Kamali Intrusive body- which is intruded and cropped out of the southern flank of Hezar strato-volcano, also is eliminated from the calculations.

no.	Sample	Location	Structure	Acidity	Isochron
8	MN130706	Babini	Lava	Basic	1
14	MN130913	Babzangi	Lava	Acidic	-
16	MN131003	Jalas	Dike	Basic	2

20	MN131017b	Kamali	Plutonic	Intermediate	-
23	MN131105	Jalas	Dike	Acidic	2
36	MN131809	Mirshadi	Lava	Intermediate	1
40	MN132108	Bozkosh	Lava	Intermediate	1

Table 2- Isotopic analyses for Rb/Sr and Sm/Nd systems for seven samples.

no.	(87Sr/86Sr)i	(143Nd/144Nd)i	EpsNdi	TDM	TDM.Gold	TDM.2stg	Age	Calculated Sr Age	Calculated Nd Age
S45	0.705828	0.512627	0.78	1.09	1.182	0.76	40	27.73557	27.47694
S51	0.706623	0.512761	3.4	0.675	0.722	0.553	40	27.65192	27.46045
S53	0.704891	0.512603	0.33	1.054	1.135	0.795	40	27.7007	28.01161
S57	0.705875	0.512635	0.95	0.909	0.973	0.746	40	27.74367	27.91025
S60	0.704516	0.512729	2.78	0.513	0.537	0.602	40	27.71576	27.70767
S73	0.70578	0.512674	1.71	0.841	0.9	0.686	40	27.74614	28.0338
S77	0.705858	0.512649	1.22	0.985	1.063	0.725	40	27.65233	27.85307

No.	**$^{87}Rb/^{86}Sr$**	**Error (2s)**	**$^{87}Sr/^{86}Sr$**	**Error (2s)**	$^{147}Sm/^{144}Nd$	**Error (2s)**	**$^{143}Nd/^{144}Nd$**	**Error (2s)**
S45	0.114	0.003	0.705893	0.000024	0.151	0.008	0.512666	0.000015
S51	0.310	0.009	0.706799	0.000018	0.139	0.007	0.512797	0.000017
S53	0.204	0.006	0.705007	0.000020	0.145	0.008	0.512641	0.000017
S57	0.568	0.016	0.706198	0.000020	0.139	0.007	0.512672	0.000016
S60	0.988	0.028	0.705077	0.000021	0.101	0.005	0.512756	0.000019
S73	0.220	0.006	0.705905	0.000023	0.139	0.007	0.512711	0.000013
S77	0.325	0.009	0.706042	0.000014	0.147	0.008	0.512688	0.000017

Table 3- Geochemical analysis of 28 rock samples using ICP-MS and XRF with calculated CIPW normative minerals.

ANALYTE	METHOD	S38	S39	S40	S41	S42	S43	S44	S45	S46	S47	S48	S49	S50	S51	S52	S53	S54	S55	S56	S57	S58	S59	S60	S61	S62	S63	S64	S65
Ag	ICM90A	0	0	0	0	0	0	0	0	0	0	2	0	0	0	4	2	2	0	0	0	3	0	0	0	0	0	2	0
As	ICM90A	0	0	22	0	0	0	0	0	0	0	11	0	7	0	0	0	0	6	0	9	15	0	0	0	0	11	0	12
Ba	ICM90A	526	355	509	335	463	533	474	364	277	401	282	365	407	621	398	183	403	446	704	310	567	923	467	311	746	415	357	389
Bi	ICM90A	0.3	0.1	0	0.2	0	0	0	0	0	0	0.1	0	0	0.8	0	0	0.2	0.1	0.2	0	0	0.4	0	0	0	0.1	0	0
Cd	ICM90A	2.9	2.3	2.5	2.3	3.6	0.4	1.1	0.9	0	0.2	1.2	1.9	1	2	1.1	1.8	1.8	2.5	1.4	2.3	1.5	1.8	0.9	2.5	1	2.2	0.6	0.8
Ce	ICM90A	53.3	64.1	83.1	48.9	52.4	41	74.8	39.2	29.9	41.7	39.5	54.8	31.5	34	60.5	35	42.1	46.7	101	53.8	24.1	73.5	50.3	42.6	40.4	81.1	40	56.9
Co	ICM90A	18.1	37.9	24.9	10.1	3.6	26.4	37.9	32.9	41.7	40.6	33.7	5.2	33.6	26.2	26.1	32	9.5	27.7	3.2	28.2	34.5	10.4	5	5.9	28.7	28.7	29.8	31.9
Cr	ICM90A	13	13	18	21	52	23	91	16	92	50	24	19	53	52	31	44	15	36	38	12	22	24	44	10	47	11	60	49
Cs	ICM90A	0.7	2.1	1.6	1.6	1.7	0.7	1.1	0.6	1.1	4.3	7	2	1	0.7	1.6	2.6	0.8	1.2	1	8.2	1.7	2.3	1.9	0.7	1.3	2	1.7	1.3
Cu	ICM90A	86	240	79	38	31	79	568	45	113	95	61	23	109	51	174	104	33	124	24	66	92	33	32	38	64	231	58	72
Dy	ICM90A	1.81	9.86	11.5	4.42	2.4	4.65	5.94	6.11	4.91	5.06	4.7	6.06	5.43	3.85	8.71	4.69	5	5.78	8.19	5.64	4.56	6.07	2.45	4.29	6.38	9.86	6.17	8.08
Er	ICM90A	0.87	6.19	7.22	2.78	1.65	2.93	3.51	3.89	3.13	3.08	3	3.9	3.49	2.44	5.34	2.94	3.2	3.56	5.91	3.62	2.9	3.95	1.74	2.89	4.05	5.99	3.84	5.18
Eu	ICM90A	1.35	2.55	3.04	1.46	1	1.66	2.37	1.95	1.59	1.81	1.44	1.62	1.49	1.18	2.18	1.56	1.75	2.3	0.97	1.8	1.58	1.49	1.04	1.59	1.88	2.33	1.7	2.06
Ga	ICM90A	20	18	16	18	12	15	13	20	15	16	15	15	16	12	18	15	17	18	14	16	15	21	12	15	15	21	16	17
Gd	ICM90A	3.34	10.1	11.9	5.24	2.78	4.92	7.03	6.15	4.79	5.34	4.91	5.89	5.27	3.66	8.78	4.91	5.19	6.15	8.29	6.03	4.46	6.97	2.9	4.5	6.28	11.2	6.22	8.2
Ge	ICM90A	0	1	1	1	1	1	1	1	1	1	1	0	1	0	0	1	0	1	0	0	0	1	1	0	0	2	0	0
Hf	ICM90A	4	6	8	5	6	4	5	4	3	3	4	7	3	5	6	3	4	4	10	5	3	8	5	5	5	8	5	6
Ho	ICM90A	0.27	1.89	2.14	0.92	0.45	0.88	1.07	1.15	0.89	0.91	0.89	1.12	1.03	0.71	1.63	0.87	0.95	1.06	1.58	1.07	0.89	1.27	0.47	0.81	1.2	2.07	1.15	1.51
La	ICM90A	29	24.6	34.4	20.1	25.3	17.1	32.6	14.5	11.5	19.1	16.5	24.8	15	22.6	26.1	15.1	19.4	21.1	52.9	25.4	9	41.8	26.7	19.7	17	36.5	16.7	24.5
Li	ICM90A	125.1	55.1	45.1	40.1	22.1	74.1	71.1	70.1	29.1	50.1	69.1	14	28	0	18	10	11	0	0	12	32	11	25	16	29	40	31	15

Lu	ICM90A	0.1	0.79	0.94	0.49	0.32	0.43	0.47	0.52	0.44	0.39	0.41	0.58	0.47	0.41	0.73	0.42	0.49	0.48	0.91	0.52	0.39	0.69	0.35	0.45	0.58	0.93	0.56	0.72
Mo	ICM90A	0	0	3	0	0	0	0	0	0	0	0	0	0	0	4	0	0	4	0	3	0	0	0	0	0	5	0	0
Nb	ICM90A	5	11	11	6	8	4	16	7	4	4	8	14	5	6	9	4	5	8	24	10	2	22	8	5	6	16	7	10
Nd	ICM90A	22.6	35.5	45.1	22.8	17.9	19.5	35	21.6	16.5	21	19.2	23.8	18	14.8	32.9	17.9	21.1	23.1	39.2	24	14	30.8	17.9	20.7	22.2	43.2	22	30.4
Ni	ICM90A	14	8	0	0	0	8	36	0	32	42	16	0	34	5	9	24	0	7	0	9	10	5	0	0	17	0	19	12
Pb	ICM90A	51	21	31	11	28	16	25	31	19	15	28	17	29	26	13	15	28	18	23	20	12	19	30	21	23	54	19	24
Pr	ICM90A	5.94	8.13	10.4	5.61	5.16	4.76	8.74	4.98	3.76	4.91	4.65	6.09	4.01	3.78	7.52	4.29	4.98	5.52	10.7	6.09	3.11	8.15	5.1	5.07	5.08	9.98	5	7.13
Rb	ICM90A	53.9	42	67.4	64.7	93.5	36.4	27.7	23.1	24.7	27.8	132	94.9	17.3	64.7	60.5	33.7	53.5	59.1	165	114	42.5	197	95.6	46	43.2	23.2	19.4	51.2
Sb	ICM90A	0.7	1.5	1	0	0	0	0	0	0	0	0.7	0	0	0	0.6	0	0	4.9	0	0	0	1.3	0	0.8	0	1.1	0	0
Sc	ICM90A	7	7	7	8	8	7	6	7	7	7	6	8	6	8	7	7	6	6	7	6	6	8	7	7	6	8	7	6
Sm	ICM90A	3.8	8.8	10.5	4.9	3	4.3	6.8	5.4	4.2	4.8	4.3	5.2	4.4	3.4	7.8	4.3	4.7	5.4	7.7	5.5	4	6.5	3	4.3	5.8	10.3	5.2	7.4
Sn	ICM90A	1	3	2	1	1	2	1	1	1	1	2	3	2	2	4	2	2	5	4	2	0	3	2	2	2	4	2	2
Sr	ICM90A	732	466	688	506	267	527	686	587	607	690	314	284	472	604	535	477	619	683	574	581	507	654	280	456	1057	643	580	617
Ta	ICM90A	1.2	1.1	1	0.7	0.8	0	1.4	0.7	0	0	0.8	1.3	0	0.6	0.8	0	0	0.7	2.4	0.9	0	1.9	0.8	0	0.6	1.2	0.6	0.9
Tb	ICM90A	0.35	1.56	1.81	0.77	0.39	0.72	1	0.94	0.77	0.81	0.74	0.91	0.83	0.57	1.36	0.76	0.78	0.89	1.23	0.9	0.74	1.03	0.38	0.67	0.98	1.67	0.96	1.28
Th	ICM90A	9.6	7.9	10.6	7.4	11.6	6.7	2.9	4.6	3.6	6.9	5.4	10.9	3.9	8.6	7.9	4.3	4.6	7.7	44.2	12.6	2.5	22	11.2	5.7	4.3	12.5	4.4	8.4
Tl	ICM90A	0	0	0	0	0	0	0	0	0	0	0.5	0	0	0	0	0	0	0	0.6	0	0	0.7	0	0	0	0	0	0
U	ICM90A	2.57	1.94	2.62	1.66	2.47	1.42	0.77	1.19	0.89	1.48	1.26	2.24	0.98	2.14	1.92	0.92	1.1	1.82	9.94	2.76	0.51	5.44	2.41	1.31	1.3	3.01	1.32	2.17
V	ICM90A	120	270	60	50	10	220	200	240	300	310	230	30	280	260	250	270	30	200	20	190	280	40	10	30	270	230	260	250
W	ICM90A	2	3	3	2	2	2	2	2	2	2	2	2	1	2	4	1	4	2	2	3	1	3	2	2	2	3	3	2
Y	ICM90A	7.5	50.1	47.9	23.7	12.3	21.6	23	31.1	21.9	21.4	24.5	32	26.2	20.4	41.7	21.1	25.5	28.1	43.8	27.3	20.6	40.4	12.6	20.1	28.6	54.8	28.1	36.1
Yb	ICM90A	0.6	4.8	5.6	3	1.8	2.6	2.8	3.1	2.5	2.4	2.4	3.4	2.8	2.3	4.3	2.4	2.9	2.8	5.4	3.1	2.4	4.3	1.8	2.6	3.3	5.8	3.2	4.2
Zn	ICM90A	100	110	130	60	50	80	90	100	100	100	120	70	90	110	110	70	100	90	10	100	80	40	50	80	100	110	90	110
OI	XRF76V	3.59	2.98	2.78	2.43	1.15	3.3	2.17	1.83	2.69	2.66	10.5	2.99	2.61	1.52	2.33	1.16	3.07	1.42	1.02	0.83	4.16	2	0.73	2.49	5.57	5.51	3.55	1.82
SiO2	XRF76V	60.5	50	55.4	60.8	71.3	54.2	51.3	49.9	49.2	47.5	46.1	67.1	49.6	68.9	51.4	50.3	58	50.9	69.2	53.7	47.7	61.7	70	60.4	49.3	52.1	51.1	51
Al	XRF76V	17.2	16.4	16.1	16.5	15.2	17.8	17.1	19.7	17	18.3	16.3	15.4	18.5	14	18.9	18.7	18.2	17.7	14.4	18.1	18	17.1	15	16.7	17.1	14.6	17.2	18.1
Fe2O3	XRF76V	4.61	12.9	10.8	4.95	1.96	8.69	10.1	10.5	11	10.9	9.38	4.23	11.1	3.96	10.5	10.1	7.48	10.9	1.89	9.93	11.5	4.75	2.09	5.13	10	11.1	10.2	10.9
MgO	XRF76V	2.2	3.09	2.18	1.56	0.45	3.59	5.11	3.11	5.52	5.39	3.58	0.92	4.97	1.2	2.79	5.27	1.55	3.22	0.55	3.29	4.73	0.99	0.45	1.28	3.08	2.82	3.87	3.42
CaO	XRF76V	4.44	8.33	5.3	4.32	1.92	5.04	8.43	9.1	9.89	9.57	8.47	2.13	9.15	2.2	8.95	9.2	6.03	8.06	2.37	8.15	8.81	3.62	2.01	4.33	6.66	7.32	8.74	8.5
K2O	XRF76V	2.29	1.75	2.89	2.01	2.9	1.62	1.78	1.13	1.07	1.34	2.93	2.29	1.03	2.91	2.22	1.28	2.17	1.88	5.02	2.26	1.45	5.36	2.8	1.79	1.95	0.98	1.13	2.06
Na2O	XRF76V	4.78	2.17	3.31	4.32	4.76	4.98	2.62	3.12	2.81	2.52	1.72	4.83	2.5	4.1	2.32	3.01	3.4	3.85	3.81	3.49	2.2	3.98	4.79	4.7	4.61	3.06	2.53	2.78
TiO2	XRF76V	0.71	1.67	1.36	0.41	0.21	0.87	1.27	1.18	1.1	1.18	0.99	0.47	1.25	0.36	1.33	1.04	0.51	1.21	0.33	1.07	1.11	0.6	0.21	0.38	1.21	1.62	1.17	1.45
MnO	XRF76V	0.07	0.21	0.21	0.14	0.09	0.18	0.16	0.15	0.18	0.19	0.2	0.09	0.18	0.07	0.15	0.17	0.17	0.21	0.02	0.18	0.19	0.06	0.14	0.17	0.16	0.2	0.17	0.18
P2O5	XRF76V	0.28	0.47	0.65	0.22	0.08	0.22	0.67	0.29	0.21	0.24	0.24	0.1	0.25	0.1	0.44	0.23	0.26	0.37	0.09	0.3	0.17	0.19	0.07	0.26	0.29	0.58	0.3	0.35
Cr2O3	XRF76V	0	0	0	0	0	0	0.02	0	0.01	0	0	0.48	0	0	0	0	0	0	0	0	0	0	0	0	0	0	0	0
V2O5	XRF76V	0.02	0.04	0.02	0	0	0.04	0.04	0.04	0.04	0.06	0.04	0	0.05	0.01	0.05	0.05	0	0.03	0	0.03	0.05	0	0	0	0.04	0.04	0.05	0.05